Comp. Appl. Math. (2014) 33:63–80
DOI 10.1007/s40314-013-0043-5

Validation of a Galerkin technique on a boundary integral equation for creeping flow around a torus

Sofía Sarraf · Ezequiel López · Gustavo Ríos Rodríguez · Jorge D'Elía

Received: 13 December 2012 / Accepted: 23 April 2013 / Published online: 21 June 2013

Abstract A validation of the numerical solution for the steady and axisymmetric creeping flow around a three-dimensional torus is presented. This solution is obtained by means of the boundary element method. Both a Galerkin weighting technique and collocation to the centroid of the elements are employed. The curve of the viscous drag force as a function of the diameter of the torus relative to its thickness is compared against a semi-analytical solution and laboratory experimental measurements taken from the literature. The semi-analytical solution, as it is known for this kind of geometry, involves the Legendre functions of first and second kind of order one and semi-integer degrees, also called toroidal harmonics.

Keywords Creeping flow · Steady flow · Boundary element method · Collocation technique · Galerkin weighting · Toroidal harmonics

Mathematics Subject Classification (2000) 65N38 · 76D07

Communicated by Gustavo Buscaglia.

S. Sarraf · E. López
Departamento de Mecánica Aplicada, Fac. de Ing., Univ. Nac. del Comahue, CONICET, Buenos Aires 1400, 8300 Neuquén, Argentina
e-mail: sssarraf@gmail.com

E. López
e-mail: ezequiel.jose.lopez@gmail.com

G. Ríos Rodríguez · J. D'Elía (✉)
Centro Internacional de Métodos Computacionales en Ingeniería (CIMEC), Instituto de Desarrollo Tecnológico para la Industria Química (INTEC), Univ. Nac. del Litoral, CONICET, Güemes 3450, 3000 Santa Fe, Argentina
e-mail: jdelia@intec.unl.edu.ar
URL: http://www.cimec.org.ar

G. Ríos Rodríguez
e-mail: gusadrr@yahoo.com.ar

1 Introduction

The computation of steady Stokes flows around closed rigid bodies can be of interest in fluid and biomedical engineering. Possible applications are multilevel boundary element method (BEM) for steady Stokes flows in irregular two-dimensional domains (Dargush and Grigoriev 2005); low Reynolds number flow of an incompressible fluid in spiral microchannels that are used in DNA identifying lab-on-a-chip devices (Lepchev and Weihs 2010); creeping flow regime in oscillatory-flow mixers with flexible chambers (Shipman et al. 2007); laminar flow in compact heat exchangers and microcoolers in electronics packaging (Galvis 2012); laminar fully developed flow in micro-/minichannels with non-circular cross sections (Tamayol and Bahrami 2010); as well as micro-electro-mechanical systems (MEMS) (Berli and Cardona 2009; Méndez et al. 2008; Wang 2002).

Indirect formulations in this flow case are commonly related to hydrodynamic double- and single-layer potentials (Ladyzhenskaya 1969; Pozrikidis 1996). An indirect Boundary Integral Equation (BIE) uses as a starting point the potentials produced by surface layers of (fictitious) singularities (Sauter and Schwab 2011). These surface singularity layers generate the physical fields of interest, which are distributed on the boundary and its intensities have to be determined such that the integrated response is equal to the prescribed boundary data. In this formulation, the physical variables of interest in the boundary value problem (BVP) are not the solution of the BIE, but they are obtained afterwards by post-treatment.

From a mathematical point of view, the unknowns in the indirect BIE are the jumps of the traces across the boundary of the Cauchy data of both the interior and the exterior BVP (Hsiao and Wendland 2008; Sauter and Schwab 2011).

Two options in the indirect BIE include the Power and Miranda (1987) and the Hebeker (1986) alternatives. In the first case, a single concentrated pair Stokeslet–Rotlet located at an interior point of the rigid body is used, while in the second case (Pozrikidis 1997), a single-layer potential is introduced, whose density $\boldsymbol{\phi}$ is proportional to the density of the double-layer potential $\boldsymbol{\psi}$. In this way, in the Hebeker alternative (Gonzalez 2009; Hebeker 1986), a completed indirect velocity BIE of Fredholm type and second kind is derived as a combination of double- and single- layer potentials with densities defined over the closed surface. It fixes the deficient range of the integral operator of a double-layer velocity potential, obtaining a well-posed problem and giving the total force and torque acting on the rigid body. The rigid body motions have been filtered assuming that the single-layer density has a linear dependence on the double-layer density.

Ingber and Mammoli (1999) showed comparisons among three alternatives:

1. the direct velocity BIE (DV-BIE) (Younggren and Acrivos 1975): a Fredholm BIE of first kind for the velocity is obtained, where the boundary conditions are given in terms of the velocity components;
2. the completed indirect velocity BIE (CIV-BIE) (Power and Miranda 1987) (or completed double-layer (CDL-BIE) Kim and Karrila 1991): the deficient range of the integral operator of the double-layer velocity potential is fixed, obtaining a well-posed problem;
3. the uncompleted direct traction BIE (UDT-BIE) (Fang et al. 2001; Ingber and Mondy 1993): the BIE for the traction is written in terms of the derivatives of the Cauchy principal value integrals, resulting in hypersingular integrals that are interpreted in the finite-part sense.

In previous works (D'Elía et al. 2008, 2012), the CIV-BIE alternative in the Hebeker (1986) scheme was chosen and solved with a BEM based on collocation and Galerkin weighting procedures, where the validation test case was restricted to the unit sphere under three inflow

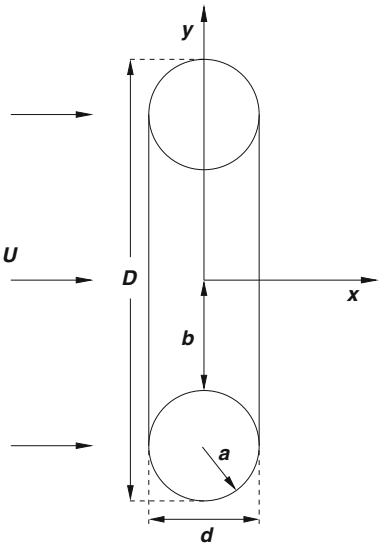

Fig. 1 Outline of the torus orientation relative to the main flow and geometrical dimensions

types. In the present work, another validation, in particular of the Galerkin technique, is performed through the axisymmetric and steady creeping flow around a three-dimensional torus. In this way, the developed method is validated for other geometries with analytical or semi-analytical solutions besides the sphere as well as oblate and prolate spheroids. The results include the numerically computed curve of the non-dimensional drag force as a function of a geometric aspect ratio parameter (s_0, see Eq. 2). This is compared with a semi-analytical solution and experimental measurements. This work extends the preliminary results presented in Sarraf et al. (2012), where only structured meshes were used and the maximum value for the geometric aspect ratio parameter was $s_0 = 100$.

2 Mathematical formulation

2.1 Differential formulation

Consider a rigid torus with outer diameter D and thickness d, located in a uniform stream of a Newtonian fluid with its symmetry axis aligned to the flow direction, as outlined in Fig. 1. The fluid flow has a constant velocity $(U, 0, 0)$ and it is assumed incompressible with constant density ρ and dynamic viscosity μ. The Reynolds number $Re = U\rho D/\mu$ is considered small enough; therefore, the following equations govern the problem:

$$\begin{aligned} \mu\nabla^2\mathbf{v} &= \nabla p \\ \nabla\cdot\mathbf{v} &= 0, \end{aligned} \tag{1}$$

where $\mathbf{v}$ is the flow velocity field and p is the pressure field. The boundary conditions that complete the problem formulation are $\mathbf{v} = \mathbf{0}$ on the surface of the torus and $\|\mathbf{v}\| \sim U$ at infinite distance from the body. The analysis is made in terms of the geometric aspect ratio parameter s_0, which is defined as

$$s_0 = (D/d) - 1 = (b/a) + 1, \tag{2}$$

where $a = d/2$ and $b = D/2 - d$ (see Fig. 1).

The problem has been studied analytically by Majumdar and O'Neill (1977), among others, and experimentally by Amarakoon et al. (1982). The particular case of the closed torus ($b = 0$) was studied by Dorrepaal et al. (1976).

2.2 Completed indirect velocity BIE

The creeping flow around a closed, rigid and piecewise smooth surface A can be computed with the Hebeker alternative (Hebeker 1986), which is an extension of the Power–Miranda proposal (Power and Miranda 1987) and it is analyzed by Pozrikidis (1996). This is written as follows

$$\int_A \tilde{K}_{ij}\psi_j(\boldsymbol{x})\mathrm{d}A_y - \int_A \tilde{H}_{ij}\psi_j(\boldsymbol{y})\mathrm{d}A_y = u_i(\boldsymbol{x}) \quad \text{for all } \boldsymbol{x} \in A, \tag{3}$$

where $\psi_j(\boldsymbol{x})$ is the double layer surface density and $u_i(\boldsymbol{x})$ are the unperturbed flow velocity components. The surface differential element is denoted by $\mathrm{d}A_y = \mathrm{d}A(\boldsymbol{y})$, while the integration and field points are $\boldsymbol{y} = (y_1, y_2, y_3)$ and $\boldsymbol{x} = (x_1, x_2, x_3)$, respectively. The double layer surface kernel $\tilde{K}_{ij} = \tilde{K}_{ij}(\boldsymbol{x}, \boldsymbol{y})$ is a tensor of rank 2 due to the surface density of stresslets distributed over the body surface (Pozrikidis 1996, 1997), and it is given by

$$\tilde{K}_{ij}(\boldsymbol{x}, \boldsymbol{y}) = -\frac{3}{4\pi\mu}\frac{r_i r_j r_k}{r^5}n_k(\boldsymbol{y}) \quad \text{with } \boldsymbol{r} = \boldsymbol{x} - \boldsymbol{y}, \text{ and } r = \|\boldsymbol{x} - \boldsymbol{y}\|_2, \tag{4}$$

where $n_k = n_k(\boldsymbol{y})$ is the unit surface normal at the integration point $\boldsymbol{y}$. For smooth surfaces, this kernel has the key property

$$\int_A \tilde{K}_{ij}(\boldsymbol{x}, \boldsymbol{y})\mathrm{d}A_y = \frac{1}{2\mu}\delta_{ij} \quad \text{for } \boldsymbol{x} \in A, \tag{5}$$

where δ_{ij} is the Kronecker delta.

On the other hand, the kernel $\tilde{H}_{ij} = \tilde{H}_{ij}(\boldsymbol{x}, \boldsymbol{y})$ is computed as

$$\tilde{H}_{ij} = \tilde{K}_{ij} + \tilde{S}_{ij}, \tag{6}$$

where $\tilde{S}_{ij} = \tilde{S}_{ij}(\boldsymbol{x}, \boldsymbol{y})$ is the sourcelet kernel given by

$$\tilde{S}_{ij}(\boldsymbol{x}, \boldsymbol{y}) = -\frac{\chi_H}{8\pi\mu}\left[\frac{\delta_{ij}}{r} + \frac{r_i r_j}{r^3}\right], \tag{7}$$

χ_H being an arbitrary positive parameter which couples the simple layer density $\boldsymbol{\phi}$ with the double layer density $\boldsymbol{\psi}$, i.e.

$$\boldsymbol{\phi}(\boldsymbol{x}) = \chi_H\, \boldsymbol{\psi}(\boldsymbol{x}). \tag{8}$$

Hebeker (1986) concludes that $\chi_H = 1$ is a good choice; therefore, this value is adopted in the present work. The kernel $\tilde{S}_{ij}(\boldsymbol{x}, \boldsymbol{y})$ is an ad-hoc auxiliary field that allows to eliminate the rigid modes and accounts for the global torque and the body force (Pozrikidis 1996).

Using matrix notation, Eq. (3) can be rewritten as

$$\mathbf{I}(\boldsymbol{x}; \boldsymbol{\psi}(\boldsymbol{x})) = \boldsymbol{u}(\boldsymbol{x}) \quad \text{for all } \boldsymbol{x} \in A; \tag{9}$$

with the integral operator

$$\mathbf{I}(\boldsymbol{x}; \boldsymbol{\psi}(\boldsymbol{x})) = \int_A \{\tilde{\boldsymbol{K}}\boldsymbol{\psi}(\boldsymbol{x}) - \tilde{\boldsymbol{H}}\boldsymbol{\psi}(\boldsymbol{y})\}\mathrm{d}A_y \quad \text{for all } \boldsymbol{x} \in A, \tag{10}$$

where the solution field is the double layer surface density $\boldsymbol{\psi}(\boldsymbol{x})$. Kernels $\tilde{\boldsymbol{H}}(\boldsymbol{x}, \boldsymbol{y})$ and $\tilde{\boldsymbol{K}}(\boldsymbol{x}, \boldsymbol{y})$ couple the double layer density $\boldsymbol{\psi}$ between the integration point $\boldsymbol{y}$ and the observation point $\boldsymbol{x}$. Equation (9) is a completed indirect velocity BIE in the Ingber–Mammoli taxonomy (Ingber and Mammoli 1999), since it does not directly provides the traction on the surface but the double layer surface density, which has been modified to eliminate the rigid modes and provides both the body force and torque.

3 Numerical formulation

3.1 Centroid collocation technique

An approximate solution to Eq. (3) can be obtained by a collocation technique, wherein the double layer surface density is assumed constant per element, resulting in the following discrete system (D'Elía et al. 2012)

$$\sum_{q=1}^{E} \left[\int_{A^{(q)}} \tilde{\boldsymbol{K}}^{(p,q)} \mathrm{d}A_y \boldsymbol{\psi}^{(p)} - \int_{A^{(q)}} \tilde{\boldsymbol{H}}^{(p,q)} \mathrm{d}A_y \boldsymbol{\psi}^{(q)} \right] = \boldsymbol{u}^{(p)}, \tag{11}$$

for $p = 1, 2, \ldots, E$, where $\tilde{\boldsymbol{H}}^{(p,q)} = \tilde{\boldsymbol{H}}(\boldsymbol{x}^{(p)}, \boldsymbol{y}^{(q)})$, $\tilde{\boldsymbol{K}}^{(p,q)} = \tilde{\boldsymbol{K}}(\boldsymbol{x}^{(p)}, \boldsymbol{y}^{(q)})$ and the vectors are $\boldsymbol{u}^{(p)} = \boldsymbol{u}(\boldsymbol{x}^{(p)})$ and $\boldsymbol{\psi}^{(p)} = \boldsymbol{\psi}(\boldsymbol{x}^{(p)})$, evaluated in the element centroids $\boldsymbol{x}^{(p)}$ by the double loop $p, q = 1, 2, \ldots, E$, while E is the element number in the BEM mesh. At the discrete level, nodal values and elements are denoted with super- and subscripts, respectively. Using matrix notation and reordering terms, it is obtained (D'Elía et al. 2012)

$$(\boldsymbol{Q} - \boldsymbol{S})\boldsymbol{\psi} = \boldsymbol{u}, \tag{12}$$

where

$$\begin{aligned} \boldsymbol{\psi} &= \left[\boldsymbol{\psi}^{(1)} \boldsymbol{\psi}^{(2)} \ldots \boldsymbol{\psi}^{(E)} \right]^{\mathrm{T}} \in \mathbb{R}^{3E \times 1}; \\ \boldsymbol{u} &= \left[\boldsymbol{u}^{(1)} \boldsymbol{u}^{(2)} \ldots \boldsymbol{u}^{(E)} \right]^{\mathrm{T}} \in \mathbb{R}^{3E \times 1} \end{aligned} \tag{13}$$

are global vectors, and $[\ldots]^{\mathrm{T}}$ denotes matrix transpose. The global matrices $\boldsymbol{Q}$ and $\boldsymbol{S}$ are given by the sums

$$\begin{aligned} \boldsymbol{Q} &= \sum_{q=1}^{E} \boldsymbol{Q}^{(p,q)}; \\ \boldsymbol{S} &= \sum_{q=1}^{E} \boldsymbol{S}^{(p,q)}; \end{aligned} \tag{14}$$

with $p = 1, 2, \ldots, E$, where

$$\boldsymbol{Q}^{(p,q)} = \begin{cases} \sum_{q=1, q \neq p}^{E} \boldsymbol{K}^{(p,q)} & \text{if } q = p; \\ -\boldsymbol{K}^{(p,q)} & \text{otherwise;} \end{cases}; \tag{15}$$

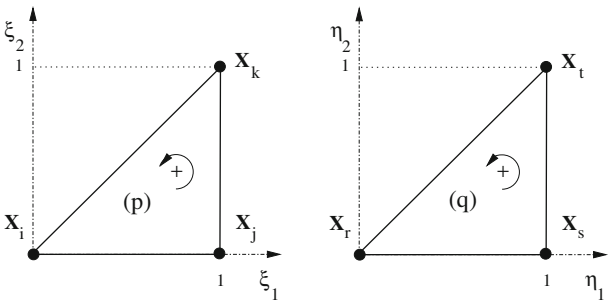

Fig. 2 Triangles p and q with simplex coordinate systems (ξ_1, ξ_2) and (η_1, η_2), respectively

whose elementary matrices are given by

$$\begin{aligned} \boldsymbol{K}^{(p,q)} &= \int_{\mathrm{A}} \tilde{\boldsymbol{K}}^{(p,q)} \mathrm{d}A_{\boldsymbol{y}}; \\ \boldsymbol{S}^{(p,q)} &= \int_{\mathrm{A}} \tilde{\boldsymbol{S}}^{(p,q)} \mathrm{d}A_{\boldsymbol{y}}. \end{aligned} \tag{16}$$

3.2 Weighted Galerkin

Another approximated solution of Eq.(3) can be obtained by means of a weighted Galerkin procedure with linear shape functions. In this case, double surface integrals with a weak singularity must be evaluated. The main ingredients are summarized below (for more details see D'Elía et al. 2012).

Over the surface of the triangles p and q, linear approximations $\hat{\boldsymbol{\psi}}^{(p,q)}$ and $\hat{\boldsymbol{u}}^{(q)}$ are chosen for the double layer density $\boldsymbol{\psi}^{(p,q)}(\boldsymbol{x}) \in \mathbb{R}^{3\times 1}$ and velocity $\boldsymbol{u}^{(q)}(\boldsymbol{x}) \in \mathbb{R}^{3\times 1}$, i.e.

$$\begin{aligned} \boldsymbol{\psi}^{(p)}(\boldsymbol{x}) \approx \hat{\boldsymbol{\psi}}^{(p)} &= \boldsymbol{N}^{(p)}(\boldsymbol{x})\boldsymbol{\psi}^{(p)} \\ \boldsymbol{\psi}^{(q)}(\boldsymbol{x}) \approx \hat{\boldsymbol{\psi}}^{(q)} &= \boldsymbol{N}^{(q)}(\boldsymbol{x})\boldsymbol{\psi}^{(q)} \\ \boldsymbol{u}^{(q)}(\boldsymbol{x}) \approx \hat{\boldsymbol{u}}^{(q)} &= \boldsymbol{N}^{(q)}(\boldsymbol{x})\boldsymbol{u}^{(q)} \end{aligned} \tag{17}$$

where the elemental shape functions $\boldsymbol{N}^{(p,q)}(\boldsymbol{x}) \in \mathbb{R}^{3\times 9}$ are given by the row vectors (by blocks)

$$\begin{aligned} \boldsymbol{N}^{(p)}(\boldsymbol{x}) &= \left[\boldsymbol{N}_i^{(p)}(\boldsymbol{x})\boldsymbol{N}_j^{(p)}(\boldsymbol{x})\boldsymbol{N}_k^{(p)}(\boldsymbol{x})\right] \\ \boldsymbol{N}^{(q)}(\boldsymbol{x}) &= \left[\boldsymbol{N}_r^{(q)}(\boldsymbol{x})\boldsymbol{N}_s^{(q)}(\boldsymbol{x})\boldsymbol{N}_t^{(q)}(\boldsymbol{x})\right] \end{aligned} \tag{18}$$

which represent the restrictions of the nodal shape functions $\boldsymbol{N}_i(\boldsymbol{x})$, $\boldsymbol{N}_j(\boldsymbol{x})$ and $\boldsymbol{N}_k(\boldsymbol{x})$ on the element p, while $\boldsymbol{N}_r(\boldsymbol{x})$, $\boldsymbol{N}_s(\boldsymbol{x})$, $\boldsymbol{N}_t(\boldsymbol{x})$ on the element q, respectively.

On the other hand, the nodal numbers in the triangles p and q are the sequences (i, j, k) and (r, s, t) traversed counterclockwise (see Fig. 2).

$$\boldsymbol{\psi}^{(p)} = \begin{bmatrix} \boldsymbol{\psi}_i \\ \boldsymbol{\psi}_j \\ \boldsymbol{\psi}_k \end{bmatrix} \in \mathbb{R}^{9\times 1} \quad \text{and} \quad \boldsymbol{\psi}^{(q)} = \begin{bmatrix} \boldsymbol{\psi}_r \\ \boldsymbol{\psi}_s \\ \boldsymbol{\psi}_t \end{bmatrix} \in \mathbb{R}^{9\times 1} \tag{19}$$

with

$$\boldsymbol{\psi}_m = \begin{bmatrix} \psi_{3m-2} \\ \psi_{3m-1} \\ \psi_{3m} \end{bmatrix} \in \mathbb{R}^{3\times 1} \tag{20}$$

while the elemental source vector is

$$\boldsymbol{u}^{(p)} = \begin{bmatrix} \boldsymbol{u}_i \\ \boldsymbol{u}_j \\ \boldsymbol{u}_k \end{bmatrix} \in \mathbb{R}^{9\times 1} \quad \text{with} \quad \boldsymbol{u}_m = \begin{bmatrix} u_{3m-2} \\ u_{3m-1} \\ u_{3m} \end{bmatrix} \in \mathbb{R}^{3\times 1} \tag{21}$$

In a standard weighting Galerkin strategy, the shape functions $\boldsymbol{N}_i(\boldsymbol{x})$ are employed to impose Eq. (9) through the orthogonality conditions

$$\int_A \boldsymbol{N}_l^{\mathrm{T}}(\boldsymbol{x})\hat{\boldsymbol{g}}(\boldsymbol{x})\mathrm{d}A_{\boldsymbol{x}} = \int_A \boldsymbol{N}_l^{\mathrm{T}}(\boldsymbol{x})\hat{\boldsymbol{u}}(\boldsymbol{x})\mathrm{d}A_{\boldsymbol{x}} \tag{22}$$

for $l = 1, 2, \ldots, N$, where N is the number of nodes of the BEM mesh. The nodal shape functions in Eq. (22) are given by

$$\boldsymbol{N}^{\mathrm{T}}(\boldsymbol{x}) = \begin{bmatrix} \boldsymbol{N}_1^{\mathrm{T}}(\boldsymbol{x}) \\ \cdots \\ \boldsymbol{N}_l^{\mathrm{T}}(\boldsymbol{x}) \\ \cdots \\ \boldsymbol{N}_N^{\mathrm{T}}(\boldsymbol{x}) \end{bmatrix} \in \mathbb{R}^{3N\times 3} \tag{23}$$

with

$$\boldsymbol{N}_l^{\mathrm{T}}(\boldsymbol{x}) = \begin{bmatrix} N_l(\boldsymbol{x}) & 0 & 0 \\ 0 & N_l(\boldsymbol{x}) & 0 \\ 0 & 0 & N_l(\boldsymbol{x}) \end{bmatrix} \tag{24}$$

for the nodes $1 \le l \le N$, with

$$N_l(\boldsymbol{x}) = \sum_{e\in \mathrm{patch}(l)} N_l^{(e)}(\boldsymbol{x}) \tag{25}$$

where patch(l) is the portion of adjacent elements around the node l. After the corresponding replacements and operations (D'Elía et al. 2012), Eq. (22) leads to the linear finite discrete system

$$\sum_{q=1}^{E} \left[\mathcal{I}^{(p,q)}\boldsymbol{\psi}^{(p)} - \mathcal{J}^{(p,q)}\boldsymbol{\psi}^{(q)} \right] = \boldsymbol{\mathcal{M}}^{(p)}\boldsymbol{u}^{(p)} \tag{26}$$

for $p = 1, 2, \ldots, E$, with the influence matrices

$$\mathcal{I}^{(p,q)} = \int_{A^{(p)}} \int_{A^{(q)}} \left[\boldsymbol{N}^{(p)T}(\boldsymbol{x})\ \boldsymbol{K}(\boldsymbol{x},\boldsymbol{y})\ \boldsymbol{N}^{(p)}(\boldsymbol{x}) \right] \mathrm{d}A_{\boldsymbol{y}}\mathrm{d}A_{\boldsymbol{x}} \tag{27}$$

and

$$\mathcal{J}^{(p,q)} = \int_{A^{(p)}} \int_{A^{(q)}} \left[\boldsymbol{N}^{(p)T}(\boldsymbol{x})\ \boldsymbol{H}(\boldsymbol{x},\boldsymbol{y})\ \boldsymbol{N}^{(q)}(\boldsymbol{y}) \right] \mathrm{d}A_{\boldsymbol{y}}\mathrm{d}A_{\boldsymbol{x}}, \tag{28}$$

and with the mass matrix

$$\mathcal{M}^{(p)} = \int_{A^{(p)}} \left[N^{(p)T}(\boldsymbol{x}) N^{(p)}(\boldsymbol{x}) \right] \mathrm{d}A_{\boldsymbol{x}} \tag{29}$$

3.3 Surface integrals over flat triangles with weak singularity

The integrals of interaction $\mathcal{I}^{(p,q)}$ and $\mathcal{J}^{(p,q)}$ given in Eqs. (27) and (28), respectively, provide a double surface integral in $\mathbb{R}^3$ like

$$\boldsymbol{Z} = \int_{A^{(p)}} \mathrm{d}A_{\boldsymbol{x}} \int_{A^{(q)}} \mathrm{d}A_{\boldsymbol{y}}\ \boldsymbol{f}(\boldsymbol{x}, \boldsymbol{y}) \tag{30}$$

on the panels p and q. In this computation, a quadruple integral is involved, whose integrand can be written as the multiplicative function $\boldsymbol{f} = \mathcal{R}\boldsymbol{G}$, where $\mathcal{R} = \mathcal{R}(\boldsymbol{x}, \boldsymbol{y})$ is a regular function and $\boldsymbol{G} = \boldsymbol{G}(r)$ is the Green function of the problem, that in this case has a weak singularity $O(1/r)$. For computing the integral in Eq. (30), two sets of coordinates are introduced, one for each simplex: (ξ_1, ξ_2) on panel p, and (η_1, η_2) on panel q (see Fig. 2):

$$\begin{aligned} (\xi_1, \xi_2) &: 0 \le \xi_1 \le 1\ ;\ 0 \le \xi_2 \le \xi_1 \\ (\eta_1, \eta_2) &: 0 \le \eta_1 \le 1\ ;\ 0 \le \eta_2 \le \eta_1 \end{aligned} \tag{31}$$

The generic points in each case are transformed into the panels p and q using the following expressions

$$\begin{aligned} \boldsymbol{x}(\xi_1, \xi_2) &= \boldsymbol{N}^{(p)}(\xi_1, \xi_2)\boldsymbol{x}^{(p)} \\ \boldsymbol{y}(\eta_1, \eta_2) &= \boldsymbol{N}^{(q)}(\eta_1, \eta_2)\boldsymbol{x}^{(q)} \end{aligned} \tag{32}$$

with the elemental shape functions

$$\begin{aligned} \boldsymbol{N}^{(p)}(\xi_1, \xi_2) &= [(1 - \xi_1)(\xi_1 - \xi_2)\xi_2] \\ \boldsymbol{N}^{(q)}(\eta_1, \eta_2) &= [(1 - \eta_1)(\eta_1 - \eta_2)\eta_2] \end{aligned} \tag{33}$$

and the elemental nodal coordinates of the vertices of each triangle

$$\boldsymbol{x}^{(p)} = \begin{bmatrix} \boldsymbol{x}_i \\ \boldsymbol{x}_j \\ \boldsymbol{x}_k \end{bmatrix} \quad ; \quad \boldsymbol{x}^{(q)} = \begin{bmatrix} \boldsymbol{x}_r \\ \boldsymbol{x}_s \\ \boldsymbol{x}_t \end{bmatrix} \tag{34}$$

Thereby, Eq. (30) is written as

$$\boldsymbol{Z} = J^{(p)} J^{(q)}\ \boldsymbol{I} \tag{35}$$

where $J^{(p),(q)} = 2A^{(p),(q)}$ are the Jacobians of each panel, and $A^{(p),(q)}$ are its areas, respectively, while $\boldsymbol{I}$ is expressed in simplices coordinates as

$$\boldsymbol{I} = \int_0^1 \mathrm{d}\xi_1 \int_0^{\xi_1} \mathrm{d}\xi_2 \int_0^1 \mathrm{d}\eta_1 \int_0^{\eta_1} \mathrm{d}\eta_2\ \boldsymbol{f}(\boldsymbol{\xi}, \boldsymbol{\eta}) \tag{36}$$

If the pairs of panels p and q are not contiguous or coincident, then the kernel in Eq. (36) is regular and, thus, a Gauss–Legendre (GL) quadrature can be applied. When the pairs have an edge or a vertex in common, weak singularities of edge or vertex, respectively, arise. If the pairs belong to the same panel, then the integration domain is weakly singular.

A systematic method to compute the surface integrals for flat simple triangular elements has been proposed by Taylor (2003a,b). The formulation is based on a suitable reordering of four iterated integrations which places the weak singularity at the origin of the four-dimensional Euclidean real space (4D or $\mathbb{R}^4$), and then applies systematically the Duffy transformation (Duffy 1982), i.e. regularizes the integrand using polar coordinates. Next, Taylor selects a GL quadrature in three of the coordinates and then performs an analytical integration in the fourth one. Since this strategy is specific for kernels of wave propagation in computational electromagnetism, a modification has been proposed in D'Elía et al. (2011). This modification consists of a numerical quadrature in the four coordinates to work with kernels with weak singularity in general. Full details about this technique can be found in D'Elía et al. (2011), Polimeridis and Mosig (2010) and Taylor (2003a), while the procedure used in the first and third reference is summarized in the following section.

3.4 Taylor scheme

The Taylor strategy to evaluate Eq. (36) is designed specifically for flat simple triangles p and q when they are contiguous or coincidents, and the integrand $\boldsymbol{f}(\boldsymbol{\xi}, \boldsymbol{\eta})$ has a weak singularity. In that case, the relative coordinates

$$\begin{aligned} \mu_1 &= \eta_1 - \xi_1 \\ \mu_2 &= \eta_2 - \xi_2 \end{aligned} \tag{37}$$

are introduced. The replacement of these coordinates into Eq. (36) leads to

$$\boldsymbol{I} = \int_0^1 \mathrm{d}\xi_1 \int_{-\xi_1}^{1-\xi_1} \mathrm{d}\mu_1 \int_0^{\xi_1} \mathrm{d}\xi_2 \int_{-\xi_2}^{\mu_1+\xi_1-\xi_2} \mathrm{d}\mu_2 \; \boldsymbol{f}(\boldsymbol{\xi}, \boldsymbol{\mu}) \tag{38}$$

Changing the integration order $(\mu_2, \xi_2, \mu_1, \xi_1)$ to the order $(\xi_2, \xi_1, \mu_2, \mu_1)$, combining integrals that have overlapping domains, and introducing several Duffy coordinate transformations, Eq. (36) is split into 3, 6 and 1 independent integrals for the common facets, common edge, and common vertex cases, respectively. It is worth to mention that the new integration order moves the weak singularity to the origin, the overlapping domains occur in the plane of the relative coordinates (μ_1, μ_2), while the Duffy coordinate transformations regularize the integrands using polar coordinates, and the selected ones are the same used by Taylor. In principle, there are six independent integrals in each case, although, with further considerations in the common facet and common vertex cases, they are reduced to 3 and 1, respectively. The final expressions are given in the next sections, where the following notations are used:

$$\begin{aligned} &\tilde{\boldsymbol{f}}_n = \tilde{\boldsymbol{f}}(\boldsymbol{\xi}_n, \boldsymbol{\eta}_n) = \boldsymbol{f}(\boldsymbol{\xi}_n, \boldsymbol{\eta}_n) + \boldsymbol{f}(\boldsymbol{\eta}_n, \boldsymbol{\xi}_n) \\ &\boldsymbol{\eta}_n = \boldsymbol{\xi}_n + \boldsymbol{\mu}_n \\ &\boldsymbol{\xi}_n, \boldsymbol{\mu}_n \;:\; \text{see each case} \end{aligned} \tag{39}$$

3.4.1 Common facets

In the case of common facets, Taylor found that the symmetry reduces the number of integrals from six to three, i.e.

$$\boldsymbol{I} = \sum_{n=1}^{3} \boldsymbol{I}_n \tag{40}$$

Table 1 Integration coordinates $\boldsymbol{\mu}_n, \boldsymbol{\xi}_n$ and Jacobian J_n, as a function of the coordinates $0 \leq \omega, x, \chi_1, \chi_2 \leq 1$ in the case of the self-integrals $\boldsymbol{I}_1 - \boldsymbol{I}_3$ (D'Elía et al. 2011; Taylor 2003a)

	$\boldsymbol{I}_1$	$\boldsymbol{I}_2$	$\boldsymbol{I}_3$
μ_1	ω	ωx	ωx
μ_2	ωx	$\omega(x-1)$	ω
ξ_1	$(1-\mu_1)\chi_1$	$(1-\mu_1+\mu_2)\chi_1 - \mu_2$	$(1-\mu_2)\chi_1 + \mu_2 - \mu_1$
ξ_2	$\xi_1\chi_2$	$(\xi_1+\mu_2)\chi_2 - \mu_2$	$(\xi_1 - \mu_2 + \mu_1)\chi_2$
J_n	$(1-\mu_1)\xi_1$	$(1-\mu_1+\mu_2)(\xi_1+\mu_2)$	$(1-\mu_2)(\xi_1 - \mu_2 + \mu_1)$

with

$$\boldsymbol{I}_n = \int_0^1 \mathrm{d}\omega \int_0^1 \mathrm{d}x \int_0^1 \mathrm{d}\chi_1 \int_0^1 \mathrm{d}\chi_2 \;\; \tilde{J}_n \tilde{\boldsymbol{f}}_n \tag{41}$$

and

$$\begin{aligned} &\omega, x, \chi_1, \chi_2 : \text{ GL quadrature points} \\ &\boldsymbol{\xi}_n = \boldsymbol{\xi}_n(\omega, x, \chi_1, \chi_2) = (\xi_1, \xi_2)_n \\ &\boldsymbol{\mu}_n = \boldsymbol{\mu}_n(\omega, x, \chi_1, \chi_2) = (\mu_1, \mu_2)_n \end{aligned} \tag{42}$$

where the intervals $0 \leq \omega, x, \chi_1, \chi_2 \leq 1$ are the usual unit interval for the GL quadrature points. The coordinates $\boldsymbol{\mu}_n$ and $\boldsymbol{\xi}_n$ are computed using rows 1–2 and 3–4 of Table 1, respectively, and the Jacobian is obtained as $\tilde{J}_n = J_a J_n$, with $J_a = \omega$, while J_n is given in the row 5 of Table 1.

3.4.2 Common edge

In the case of a common edge, six integrals must be computed, i.e.

$$\boldsymbol{I} = \sum_{n=4}^{9} \boldsymbol{I}_n \tag{43}$$

with

$$\boldsymbol{I}_n = \int_0^1 \mathrm{d}\omega \int_0^1 \mathrm{d}x_1 \int_0^1 \mathrm{d}x_2 \int_0^1 \mathrm{d}\chi_1 \;\; \tilde{J}_n \tilde{\boldsymbol{f}}_n \tag{44}$$

and

$$\begin{aligned} &\omega,\ x_1\ , x_2, \chi_1 : \text{GL quadrature points} \\ &\boldsymbol{\xi}_n\ = \boldsymbol{\xi}_n(\omega, x_1, x_2, \chi_1) = (\xi_1, \xi_2)_n \\ &\boldsymbol{\mu}_n\ = \boldsymbol{\mu}_n(\omega, x_1, x_2, \chi_1) = (\mu_1, \mu_2)_n \end{aligned} \tag{45}$$

where the intervals $0 \leq \omega, x_1, x_2, \chi_1 \leq 1$ are the usual unity interval for the GL quadrature points. The coordinates $\boldsymbol{\mu}_n$ and $\boldsymbol{\xi}_n$ are computed using columns 1–2 and 3–4 of Table 2, respectively, and the Jacobian is obtained as $\tilde{J}_n = J_b \overline{J}$, with $J_b = x_1\omega^2$ and $\overline{J} = 1 - \omega$.

Table 2 Integration coordinates $\boldsymbol{\mu}_n$ and $\boldsymbol{\xi}_n$, as a function of the coordinates $0 \leq \omega, x_1, x_2, \chi_1 \leq 1$ in the integrals with a common edge $\boldsymbol{I}_4 - \boldsymbol{I}_9$ (D'Elía et al. 2011; Taylor 2003a)

	μ_1	μ_2	ξ_1	ξ_2
$\boldsymbol{I}_4$	$-\omega x_1$	$-\omega x_1 x_2$	$(1-\omega)\chi_1 + \omega$	$\omega(1 - x_1 + x_1 x_2)$
$\boldsymbol{I}_5$	ωx_1	$\omega x_1 x_2$	$(1-\omega)\chi_1 + \omega(1 - x_1)$	$\omega(1 - x_1)$
$\boldsymbol{I}_6$	$-\omega x_1 x_2$	$\omega x_1(1 - x_2)$	$(1-\omega)\chi_1 + \omega$	$\omega(1 - x_1)$
$\boldsymbol{I}_7$	$\omega x_1 x_2$	$\omega x_1(x_2 - 1)$	$(1-\omega)\chi_1 + \omega(1 - x_1 x_2)$	$\omega(1 - x_1 x_2)$
$\boldsymbol{I}_8$	$-\omega x_1 x_2$	$-\omega x_1$	$(1-\omega)\chi_1 + \omega$	ω
$\boldsymbol{I}_9$	$\omega x_1 x_2$	ωx_1	$(1-\omega)\chi_1 + \omega(1 - x_1 x_2)$	$\omega(1 - x_1)$

Table 3 Integration coordinates $\boldsymbol{\xi}_{10}$ and $\boldsymbol{\eta}_{10}$, as a function of the coordinates $0 \leq \omega, z_1, z_2, z_3 \leq 1$ in the integral with a common vertex $\boldsymbol{I}_{10}$ (D'Elía et al. 2011; Taylor 2003a)

	ξ_1	ξ_2	η_1	η_2
$\boldsymbol{I}_{10}$	ω	ωz_1	ωz_2	$\omega z_2 z_3$

3.4.3 Common vertex

Finally, in the case of a common vertex, the six integrals are reduced to one, i.e.

$$\boldsymbol{I}_{10} = \int_0^1 \mathrm{d}\omega \int_0^1 \mathrm{d}z_1 \int_0^1 \mathrm{d}z_2 \int_0^1 \mathrm{d}z_3 \;\; \tilde{J_{10}} \tilde{\boldsymbol{f}}_{10} \tag{46}$$

and

$$\begin{aligned} \omega,\ z_1\ , z_2, z_3 &: \text{ GL quadrature points} \\ \boldsymbol{\xi}_{10} &= \boldsymbol{\xi}_{10}(\omega, z_1, z_2, z_3) = (\xi_1, \xi_2)_{10} \\ \boldsymbol{\eta}_{10} &= \boldsymbol{\eta}_{10}(\omega, z_1, z_2, z_3) = (\eta_1, \eta_2)_{10} \end{aligned} \tag{47}$$

where the intervals $0 \leq \omega, z_1, z_2, z_3 \leq 1$ are the usual unity interval for the GL quadrature points. The coordinates $\boldsymbol{\xi}_{10}$ and $\boldsymbol{\eta}_{10}$ are computed using columns 1–2 and 3–4 of Table 3, respectively, and the Jacobian is obtained as $\tilde{J_{10}} = J_c$, with $J_c = z_2 \omega^3$.

3.5 Traction field on the surface

The force $\mathbf{F} = (F_x, F_y, F_z)$ and the torque $\mathbf{T} = (T_x, T_y, T_z)$ about the origin $O(x, y, z)$ of the cartesian coordinate system acting on the body are calculated as a postprocessing through surface integrals (Power and Miranda 1987)

$$\begin{aligned} \mathbf{F} &= \int_A \mathrm{d}A_{\boldsymbol{y}}\ \boldsymbol{\psi}; \\ \mathbf{T} &= \int_A \mathrm{d}A_{\boldsymbol{y}}\ (\boldsymbol{r} \times \boldsymbol{\psi}). \end{aligned} \tag{48}$$

The traction field over the body surface is the superposition of the tractions caused by the simple and double layer potentials. The direct value of these tractions (on the body surface)

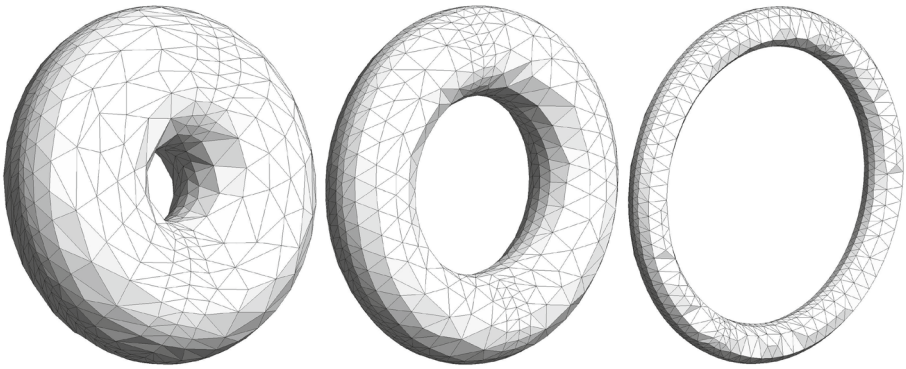

Fig. 3 Mesh of flat triangles for the cases $s_0 = 1.5$, 3 and 8, respectively

can be obtained by means of the calculation of a boundary integral, which is weakly singular in the first case and hypersingular in the second one (Gonzalez 2009). Since this work is oriented to a numerical scheme for the first case, then as a first approximation, only the contribution of the single layer potential is computed.
Therefore, the traction field $t_i(\boldsymbol{x})$ on the surface A is calculated with the BIE (Ladyzhenskaya 1969)

$$t_i(\boldsymbol{x}) = -\frac{3}{4\pi}\int_A \mathrm{d}A_y \frac{r_i r_j r_k}{r^5} n_j(\boldsymbol{x})\psi_k(\boldsymbol{y}) \quad \text{for all } \boldsymbol{x} \in A; \tag{49}$$

In Eq. (49), it is assumed that the unit normal $\boldsymbol{n}$ is well defined at the field point $\boldsymbol{x}$. This restriction prevents the use of this equation to compute the traction field at points of geometric discontinuity, like nodes, edges or vertices of the surface mesh. Hence, the centroids of the panels are used like field points $\boldsymbol{x}$ in the solved examples. Finally, the force obtained by integrating the traction field given by Eq. (49) matches with that obtained with Eq. (48).

4 Numerical results

In this section, the numerical results of Eq. (9) for both, Galerkin and collocation, are presented. In the whole set of cases, it was adopted: exterior diameter $D = 1$ m, fluid density $\rho = 1$ kg/m^3, dynamic viscosity $\mu = 1$ Pa s, and undisturbed speed $U = 1 \times 10^{-3}$ m/s. Values for the geometric aspect ratio parameter s_0 were chosen in the interval (1, 300].

The discretization of the torus surface was performed using structured and unstructured meshes of flat triangles. Figure 3 shows the unstructured surface mesh used for some values of the geometric aspect ratio parameter s_0.

In the case of structured meshes, the generating circumference is divided into n elements of equal length $h = \pi d/n$. In the perpendicular direction to this circumference, the torus surface is uniformly discretized dividing the outer circle in m segments with length $H = \pi D/m$. Then, each quadrangle of the resulting mesh is divided by one of its diagonals into two triangles. This discretization leads to the collapse of panels when $s_0 = 1$ (closed torus). Therefore, in order to avoid the collapse of panels, the case $s_0 = 1$ was actually solved taking $s_0 = 1 + \varepsilon$, with $\varepsilon = 1 \times 10^{-4}$. As the parameter s_0 increases,

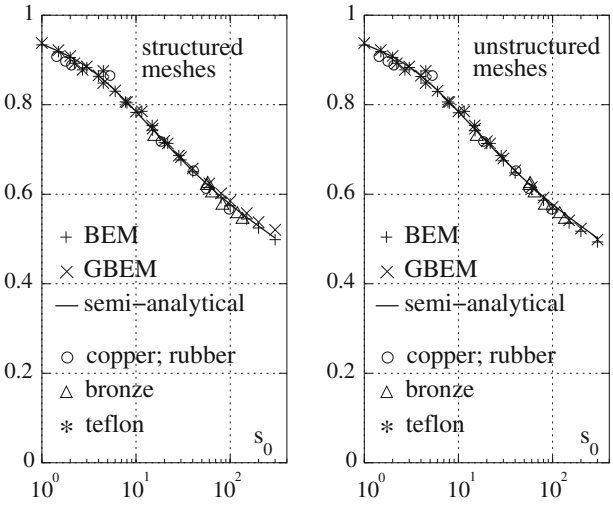

Fig. 4 Non-dimensional drag force F_∞ as a function of the geometric aspect ratio parameter s_0. Experimental points obtained in Amarakoon et al. (1982), semi-analytical and numerical solutions, by collocation (*BEM*) and Galerkin (*GBEM*), on structured (*left*) and unstructured meshes (*right*)

the torus decreases its thickness (see Eq. 2), which deteriorates the element aspect ratio. The effect of this deterioration can be mitigated by redefining the discretization (increasing m and, simultaneously, decreasing n) or directly by increasing the element number along the outer circle (m). The last option is not viable due to the increase in the computational cost, particularly for large values of s_0. Therefore, in this work, it was adopted as criterion to redistribute the panels maintaining constant its number. This approach is useful for mesh convergence study. Then, for a mesh with E panels, the discretization is chosen such that the aspect ratio h/H does not decrease below a prescribed value α, having

$$\begin{cases} n = \max\left[\sqrt{\frac{E}{\alpha(s_0+1)}},\ 4\right] \\ mn = E \end{cases} \tag{50}$$

In this work, $\alpha = 0.2$ was used.

All numerical examples were performed using $n_{1d} = 2$ GL points in each integration coordinate.

4.1 Drag curve

According to Amarakoon et al. (1982), the results for the drag are expressed in terms of the drag on a sphere with the same outer diameter as the torus, which allows to define the following non-dimensional parameter

$$F_\infty = \frac{F}{3\pi\mu U D}, \tag{51}$$

where F is the modulus of the drag force over the torus.

Figure 4 shows the non-dimensional drag force F_∞ as a function of the geometric aspect ratio parameter s_0 computed by collocation and GBEM, and using structured and unstructured

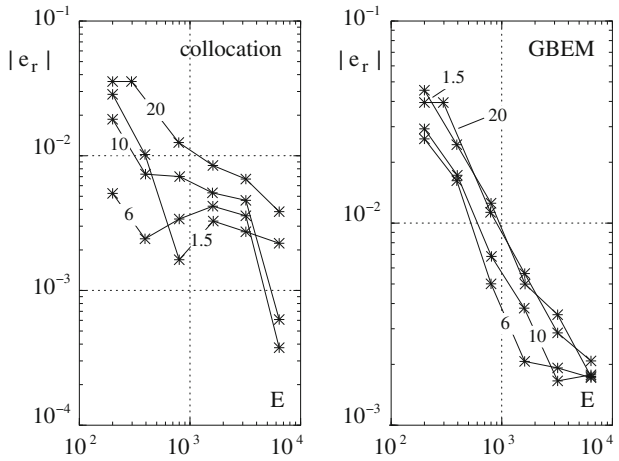

Fig. 5 Relative error for the non-dimensional drag force as a function of the number of panels E for different values of the geometric aspect ratio parameter s_0. Numerical results obtained with structured meshes, using collocation (*left*) and Galerkin (*right*)

meshes. The numerical results presented in Fig. 4 were obtained using a mesh with 6,400 elements. In this figure, a semi-analytical solution obtained by Majumdar and O'Neill (1977) and experimental results by Amarakoon et al. (1982) are also included. The agreement of the numerical results with the semi-analytical ones is very good. The weighted Galerkin method presents better results than collocation for high values of the geometric aspect ratio parameter s_0, particularly when structured meshes are used.

4.2 Mesh convergence

The relative error for the non-dimensional drag force is shown in Fig. 5 for the case of structured meshes, using collocation (left) and Galerkin (right). The relative error is defined as $e_r = |F_\infty^n - F_\infty^{\text{sa}}|/F_\infty^{\text{sa}}$, where F_∞^n is the force computed with the numerical solution and F_∞^{sa} is the semi-analytical value. Figure 5 presents the variation of the relative error for several values of the geometric aspect ratio parameter s_0. The analogous results for the solution obtained with unstructured meshes are presented in Fig. 6.

In general, the Galerkin method exhibits a monotonous reduction of the error. This feature is not verified for the collocation technique, for which the behavior of the relative error is somewhat erratic.

4.3 Computational cost

Figure 7 (left) shows the elapsed total time, in seconds, as a function of the number of elements E for both collocation (BEM) and weighted Galerkin (GBEM), using the same direct solver (Householder method) in four of the six cores of a Xeon W3690 processor. Figure 7 (right) shows the main computer memory (read/write RAM, in [GB]) used comparing BEM with GBEM. Note that classic BEM with collocation becomes impracticable, whereas with GBEM values of M relatively higher can be considered. This is because $M = 3E$ in BEM and $M = 3N$ with GBEM, where usually $E \gg N$ in 3D problems. Besides, although the system matrix is dense in both cases, it is symmetric only for Galerkin.

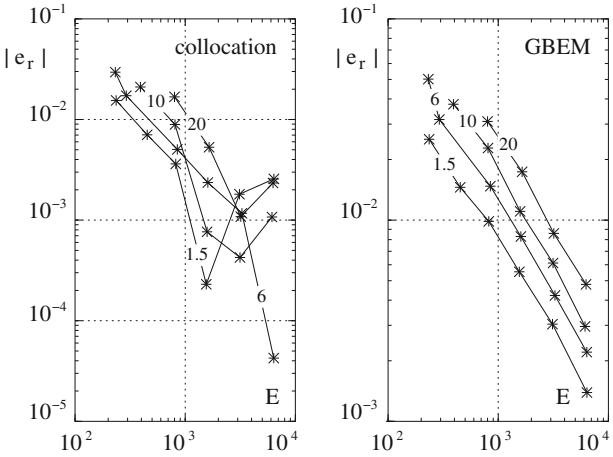

Fig. 6 Relative error for the non-dimensional drag force as a function of the number of panels E for different values of the geometric aspect ratio parameter s_0. Numerical results obtained with unstructured meshes, using collocation (*left*) and Galerkin (*right*)

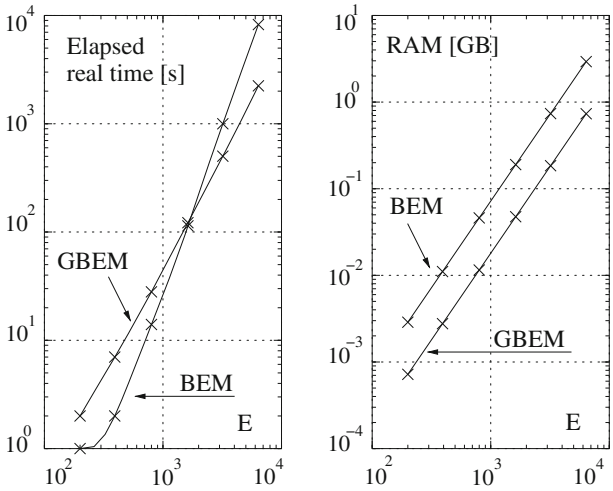

Fig. 7 Computational cost as a function of the number of elements obtained by a quasi-uniform refinement. Total time of computation [s] (*left*) and read/write RAM [GB] (*right*), collocation (*BEM*) versus weighted Galerkin (*GBEM*), with the same direct solver (Householder method) using four of the six cores of a Xeon W3690 processor

Figure 8 shows the number of pairs of interacting integration points $\times 10^6$ as a function of the number of elements E using collocation (BEM, left) and weighted Galerkin (GBEM, right) in the case of structured meshes. In this figure, the number of interactions is divided into: z_{pp} for common facets (auto-interactions), z_{pq} for non-common facets, $z_{\text{c-edge}}$ for facets with a common edge, and $z_{\text{c-vertex}}$ for facets with a common vertex.

The number of pairs of interacting integration points is given by $z = M^2 n_{1d}^2$ and $z = \hat{M}^2 n_{1d}^4$ for collocation and weighted Galerkin, respectively, where $M = 3E$ and $\hat{M} = 3N$ are the number of degrees of freedom in each case, while n_{1d} is the number of GL points in

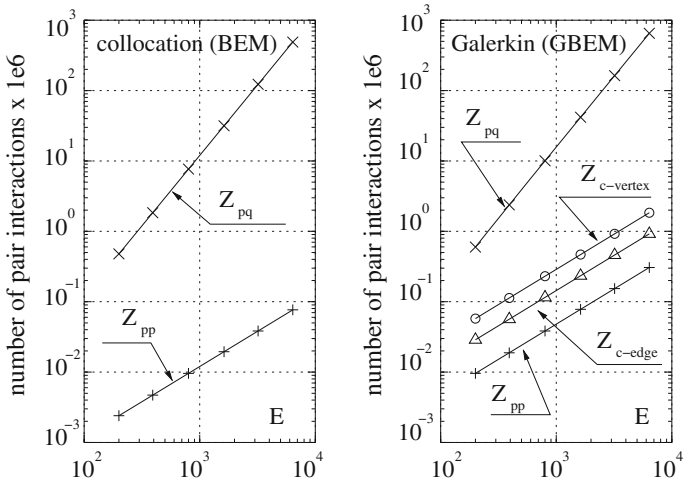

Fig. 8 Number of pairs of interacting integration points $\times 10^6$ as a function of the number of elements E using collocation (BEM, *left*) and weighted Galerkin (GBEM, *right*) in the case of structured meshes. The number of interactions is divided into z_{pp}: common facets (or auto-interactions); z_{pq}: non-common facets; $z_{\mathrm{c-edge}}$: facets with a common edge; and $z_{\mathrm{c-vertex}}$: facets with a common vertex

each integration coordinate. Each pair integration in BEM is a double integral and in GBEM is a quadruple one; therefore, there are n_{1d}^2 and n_{1d}^4 evaluations per each pair of interaction in each case.

5 Conclusions

In this work, a weighted Galerkin and a collocation technique were validated on a boundary integral equation for a numerical solution of the BVP related to a steady and axisymmetric creeping flow around a three-dimensional torus. The BIE employed was one of Fredholm type and second kind with a weak singularity, obtained with the Hebeker alternative in an indirect formulation, where single and double density layers were combined in such a way that the spectrum of the integral operator was completed and the rigid modes were excluded, while the source term was given by the no-slip boundary condition for the velocity on the body surface. This is equivalent to a completed indirect velocity BIE (CIV-BIE). The discrete linear systems were obtained using constant and linear shape functions, for collocation and Galerkin weighting, respectively, on a polyhedral approximation of the body surface composed by flat simple triangles. The matrix systems obtained with both methods were dense and regular, although only in the Galerkin case it was also symmetric, and a direct solver was used for solving them. In the numerical tests, performed as a function of the geometric aspect ratio parameter s_0, the drag curve was traced by points for both, structured and unstructured meshes, showing no differences between collocation and Galerkin weighting, with zero force, to machine accuracy, of the components in the directions perpendicular to the flow. Both methods showed mesh convergence and they were able to solve the present flow problem from a very closed torus ($s_0 = 1 + 10^{-4}$) up to a very open one ($s_0 = 300$), although Galerkin weighting showed better results for high values of the geometric aspect ratio parameter s_0 and a better mesh convergence. This was evidenced in the drag curves, where the curve obtained with a collocation

technique deviates from the semi-analytical one for high values of the geometric aspect ratio parameter s_0. Nevertheless, the errors in the drag curve were lower than 1.5 %, compared with the semi-analytical solution, as well as they are well compared with the experimental tests.

Acknowledgments This work has received financial support from Consejo Nacional de Investigaciones Científicas y Técnicas (CONICET, Argentina, grant PIP 112-20111-00978), Universidad Nacional del Litoral (UNL, Argentina, Grant CAI+D 2009-III-4-2), Agencia Nacional de Promoción Científica y Tecnológica (ANPCyT, Argentina, grants PICT 2010-2492/16, PICT 2009-1141/07, PICT-PRH 2009-0147), EU-IRSES (PIRSES-GA-2009-246977), and was performed with the *Free Software Foundation /GNU-Project* resources such as GNU-Linux-OS, GNU-GFortran, GNU-Octave, GNU-Git, GNU-Doxygen, and GNU-GIMP, as well as other Open Source resources as NETGEN, ParaView, OpenDX, Xfig and LATEX.

References

Amarakoon AMD, Hussey RG, Good BJ, Grimsal EG (1982) Drag measurements for axisymmetric motion of a torus at low Reynolds number. Phys Fluids 25(9):1495–1501

Berli C, Cardona A (2009) On the calculation of viscous damping of microbeam resonators in air. J Sound Vib 327(1–2):249–253

Dargush GF, Grigoriev MM (2005) Fast and accurate solutions of steady Stokes flows using multilevel boundary element methods. J Fluids Eng Trans ASME 127(4):640–646

D'Elía J, Battaglia L, Cardona A, Franck G (2012) Galerkin boundary elements for a computation of the surface tractions in exterior Stokes flows. Technical report, CIMEC-INTEC, UNL-CONICET

D'Elía J, Battaglia L, Cardona A, Storti M (2011) Full numerical quadrature of weakly singular double surface integrals in Galerkin boundary element methods. Int J Numer Methods Biomed Eng 27(2):314–334. doi:10.1002/cnm.1309

D'Elía J, Battaglia L, Storti M, Cardona A (2008) Galerkin boundary integral equations applied to three dimensional Stokes flows. In: Cardona A, Storti M, Zuppa C (eds) Mecánica Computacional, vol XXVII. San Luis, pp 2397–2410

Dorrepaal JM, Majumdar SR, O'Neill ME, Ranger K (1976) A closed torus in Stokes flow. Q J Mech Appl Math 29(381)

Duffy MG (1982) Quadrature over a pyramid or cube of integrands with a singularity at a vertex. SIAM J Numer Anal 19(6):1260–1262

Fang Z, Mammoli AA, Ingber MS (2001) Analyzing irreversibilities in Stokes flows containing suspensed particles using the traction boundary integral equation method. Eng Anal Bound Elements 25:249–257

Galvis E, Yarusevych S, Culham JR (2012) Incompressible laminar developing flow in microchannels. J Fluids Eng Trans ASME 134(1): 014, 503

Gonzalez O (2009) On stable, complete, and singularity-free boundary integral formulations of exterior Stokes flow. SIAM J Appl Math 69:933–958

Hebeker FK (1986) Efficient boundary element methods for three-dimensional exterior viscous flow. Numer Methods PDE 2(4):273–297

Hsiao GC, Wendland WL (2008) Boundary integral equations. Springer, Berlin

Ingber MS, Mammoli AA (1999) A comparison of integral formulations for the analysis of low Reynolds number flows. Eng Anal Bound Elements 23:307–315

Ingber MS, Mondy LA (1993) Direct second kind boundary integral formulation for Stokes flow problems. Comput Mech 11:11–27

Kim S, Karrila SJ (1991) Microhydrodynamics: principles and selected applications. Butterworth-Heinemann, UK

Ladyzhenskaya OA (1969) The mathematical theory of viscous incompressible flow, 2nd edn. Gordon and Breach Science Publishers, New York

Lepchev D, Weihs D (2010) Low Reynolds number flow in spiral microchannels. J Fluids Eng Trans ASME 132(7):071202

Majumdar SR, O'Neill ME (1977) On axisymmetric Stokes flow past a torus. Z Angew Math Phys 28(4):541–550

Méndez C, Paquay S, Klapka I, Raskin JP (2008) Effect of geometrical nonlinearity on MEMS thermoelastic damping. Nonlinear Anal R World Appl 10(3):1579–1588

Polimeridis AG, Mosig JR (2010) Complete semi-analytical treatment of weakly singular integrals on planar triangles via the direct evaluation method. Int J Numer Methods Eng 83(12):1625–1650

Power H, Miranda G (1987) Second kind integral equation formulation of Stokes flows past a particle of arbitrary shape. SIAM J Appl Math 47(4):689–698
Pozrikidis C (1996) Introduction to theoretical and computational fluid dynamics. Oxford University Press, Oxford
Pozrikidis C (1997) Boundary integral and singularity methods for linearized viscous flow. Cambridge University Press, Cambridge
Sarraf S, López E, Ríos Rodríguez G, D'Elía J (2012) Simulación del flujo reptante exterior a un toro tridimensional mediante el método de elementos de borde. In: Cardona A, Kohan PH, Quinteros RD, Storti MA (eds) Mecánica Computacional, vol XXXI. Salta, Argentina, pp 321–332
Sauter SA, Schwab C (2011) Boundary element methods. Springer, Berlin
Shipman TN, Prasad AK, Davidson SL, Cohee DR (2007) Particle image velocimetry evaluation of a novel oscillatory-flow flexible chamber mixer. J Fluids Eng Trans ASME 129(2):179–187
Tamayol A, Bahrami M (2010) Laminar flow in microchannels with noncircular cross section. J Fluids Eng Trans ASME 132(11):111, 201
Taylor DJ (2003a) Accurate and efficient numerical integration of weakly singulars integrals in Galerkin EFIE solutions. IEEE Trans Antennas Propag 51(7):1630–1637
Taylor DJ (2003b) Errata to "Accurate and efficient numerical integration of weakly singulars integrals in Galerkin EFIE solutions". IEEE Trans Antennas Propag 51(9):2543–2543
Wang X (2002) Fast Stokes: a fast 3-D fluid simulation program for micro-electro-mechanical systems. PhD thesis. MIT, Cambridge
Younggren GK, Acrivos A (1975) Stokes flow past a particle of arbitrary shape: a numerical method of solutions. J Fluid Mech 69(2):377–403